Bulletin of the Seismological Society of America, Vol. 87, No. 4, pp. 987–998, August 1997

Approximation of Rupture Directivity in Regional Phases Using Upgoing and Downgoing Wave Fields

by Chandan K. Saikia and D. V. Helmberger

Abstract Recent broadband modeling of regional events suggests that vertical directivity is particularly important at high frequency. Conventionally, such directivity is obtained by summing a grid of point sources. This relatively time-consuming procedure can be greatly reduced by introducing directivity time histories appropriate for the various crustal phases in terms of upgoing and downgoing paths that are calculated at only one depth. To achieve this, we formulated frequency-wavenumber solutions for a simultaneous computation of surface displacement for three wave fields, upgoing, downgoing, and the total from a seismic source buried in a layered medium (Appendix A). The concept of upgoing and downgoing wave field is introduced in the source layer matrix explicitly before allowing the source coefficients to interact with the propagation of the stress-displacement vector. Using this new algorithm, we generated a set of upgoing and downgoing wave fields at a fixed depth for different crustal models. We also simulated the effects of rupture propagation using distributed point-source summations and predicted the same effect by summing the upgoing and downgoing wave fields calculated at a single depth, each convolved with a separate analytical boxcar function representing the far-field rupture. A library of these new Green's functions should prove much more effective in modeling recorded motions than using point-source Green's functions alone.

Introduction

Recent broadband modeling of local and regional seismograms has demonstrated that waveform modeling techniques are successful in retrieving source parameters of earthquakes (Zhao and Helmberger, 1993; Saikia and Helmberger, 1993; Saikia *et al.,* 1996; Zhu and Helmberger, 1996). While long-period waveforms are useful for extracting point-source parameters, high-frequency signals are useful for examining the complicated effects involved in rupture directivity (Savage, 1965, 1966; Dreger and Helmberger, 1991; Dreger, 1994). The problem with the point-source solution is that it is not an unambiguous identification of the rupture plane. For events occurring on a previously unmapped fault, the identity of fault planes remains ambiguous unless aftershocks are located and depth cross sections are studied. For example, the rupture plane of the Northridge earthquake of 17 January 1994 could be resolved only after the aftershocks were located and depth cross sections were studied (Hauksson *et al.,* 1994). In this article, we outline an approximate method that can provide helpful tools to examine source finiteness in small earthquakes by analyzing high-frequency waveforms. To summarize briefly, we use upgoing and downgoing wave fields only at one depth, which is the main advantage, and convolve each wave field with a time function based on the rupture process (Langston, 1978), producing seismograms replicating the principal features of the rupture process recorded on seismograms. Since we use wave fields at one depth, it has advantage over other approaches that need wave fields on many points on the fault surface. To compute the upgoing and downgoing wave fields, we use the frequency-wavenumber integration scheme (Bouchon, 1981; Saikia, 1994; Wang and Herrmann, 1980) and modify the $F(k, \omega)$ kernel of the total wave field (Saikia, 1994) that is discussed in Appendix A. In Appendix B, we validate our partitioned wave fields by comparing against the generalized ray analysis.

In Figure 1, we present a set of three-component regional synthetic seismograms for a strike-slip fault for a vertically propagating rupture front using six equidistant point sources, each having a seismic moment of 10^{23} dyne-cm. We distribute these sources within 7 and 12 km depths. In the top panel, the bottom three seismograms correspond to the case when the rupture just initiates at a depth of 12 km. The remaining seismograms show the cumulative wave field for the rupture front propagating to other depths, as indicated to the left of each waveform plotted in the leftmost column. The dotted lines indicate the depth-dependent move out of various regional phases, such as P_n, *PmP, sPmP, pPmP, SmS, pSmS, sSmS,* direct *SH, SHmSH,* and *sSHmSH* as in-

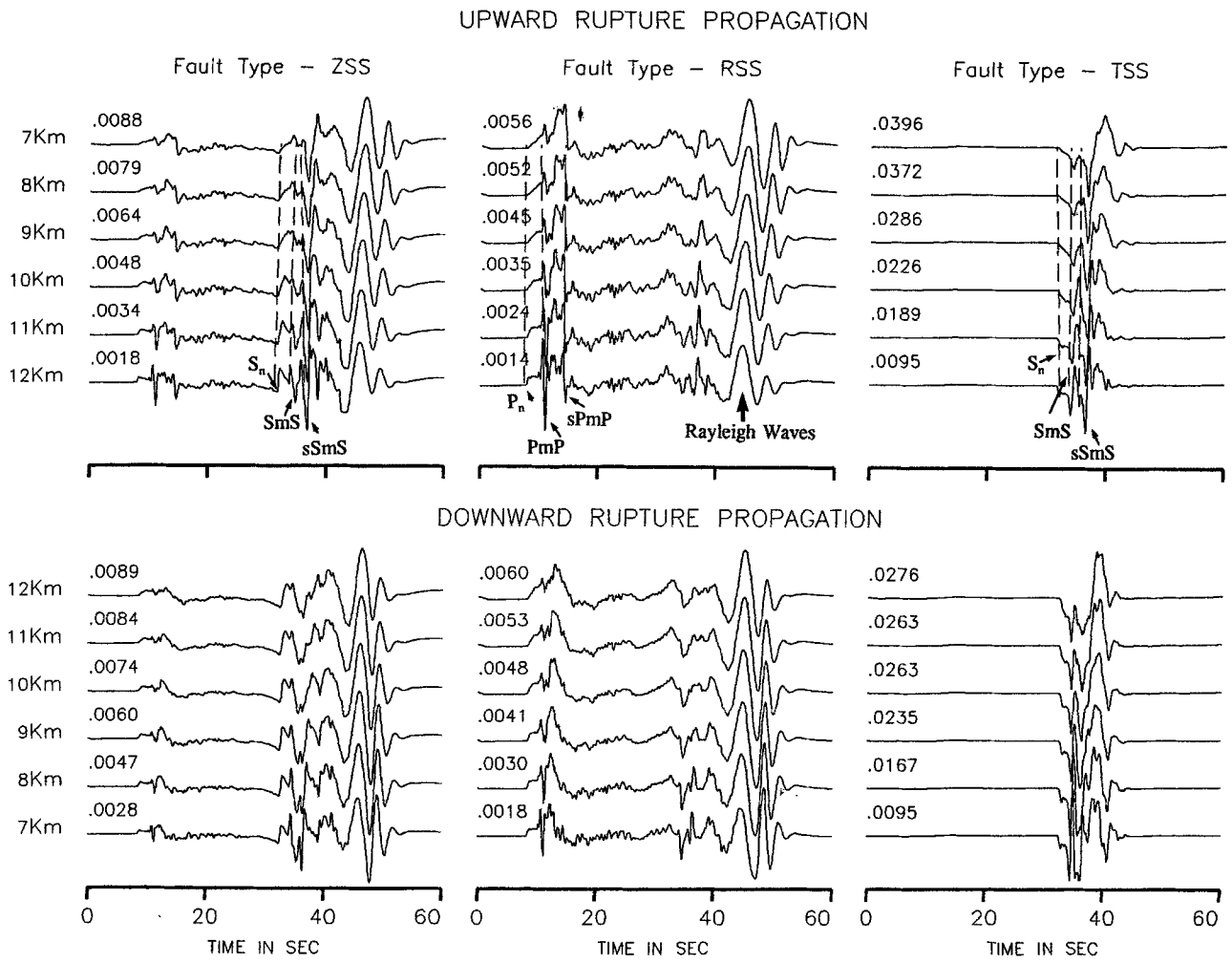

Figure 1. Upper traces in each panel show the rupture effect simulated for a strike-slip earthquake by summing point sources. The lower seismograms show the cumulative rupture effect when the rupture front reaches a particular depth, indicated to the left of each seismogram. Six point sources are summed, each with $M_0 = 10^{23}$ dyne-cm and a slip function represented by a trapezoid (0.2, 0.2, and 0.2 sec). The dotted lines show the move out of various regional phases.

fluenced by the rupture process. For example, the two distinct phases that follow the *P* onset in the upper panel for the upward rupture are *PmP* and *sPmP* waves, the *PmP* starting strongly at the rupture initiation but becoming weak compared to this *sPmP* as the rupture continues to propagate upward. The reason for the strong *sPmP* is that they arrive within a short time window and interfere constructively during the upward rupture propagation. The *PmP* waves do just the opposite. For the downward rupture that initiates at 7 km, *sPmP* has a longer effective duration because the arrivals from the adjacent sources have broader time separations. These principal features are observed in many seismograms and can be inverted to understand the rupture process during an earthquake. For example, Helmberger *et al.* (1992) were able to find evidence for a similar type of rupture effect in the Coyote Mountain earthquake data that they modeled by assuming propagation along a line of six events.

Theory for a Finite Propagating Source

Generally, earthquakes are produced by shear faulting that begins presumably at a point or in a small region and spreads outward on the fault surface. For shallow-focus events, the upward extent is limited by the free surface, and the downward extent is limited by the frictional condition. In general, the far-field response, $O(t)$, of a propagating rupture dislocation along a vertical line fault can be represented by a simple convolution of a boxcar function of duration t_R with a step response $I(t)$. The parameter t_R represents the time needed by the rupture front to propagate from the nu-

cleation to its stoppage. Mathematically, $O(t)$ is expressed as

$$O(t) = I(t) * [H(t) - H(t - t_R)]/t_R, \quad (1)$$

$H(t)$ being a Heavyside step function. The far-field response for a propagating step dislocation over a rectangular fault, which is evaluated at a receiver point P (spherical polar coordinates r, Θ, Φ) from a rupture over a finite fault that lies on the $Y = 0$ plane bounded between $-a$ and $+a$ along the X direction and from 0 to b along the Z direction (Fig. 2), is expressed by

$$s(t,r) = \int_0^b \int_{-a}^{+a} w(x,z)\, \delta\left(t - \frac{z}{v_r} - \frac{r}{v_a}\right) dx dz, \quad (2)$$

where v_r and v_a are the rupture and apparent velocities, respectively; $w(x, y)$ is the weighting slip factor at a given point on the fault. For a uniform slip model and constant apparent velocity, integrating along the x axis from $-a$ to $+a$ and along the z axis from 0 to b, the above integral reduces to

$$s(t,r) = \frac{1}{q_1 q_2} [R(\tau + q_1 a) - R(\tau - q_1 a) - R(\tau - q_2 b + q_1 a) + R(\tau - q_2 b - q_1 a)] \quad (3)$$

(Langston, 1978), where $R(t)$ is a ramp function, $\tau = t - r_0/v_a$ and q_1 and q_2 are as follows:

$$q_1 = \frac{\sin\theta \sin\phi}{v_a} \qquad q_2 = \frac{1}{v_r} - \frac{\sin\theta \cos\phi}{v_a}.$$

The time function representing the rupture propagation on a fault surface with a uniform slip distribution is a ramp that follows from (2). Hence, this ramp function should be convolved with the step response of the medium to incorporate this rupture effect. In this study, we restrict the rupture process to a vertical line fault as in Figure 1, and so, the x dependence in (2) can be dropped. For the time being, we also assume that the apparent velocity varies slowly with depth so that it can be treated as constant, thus reducing the expression (2) to

$$\frac{1}{q_2} H(\tau) - H\left[\tau - b\left(\frac{1}{v_r} - \frac{\sin\theta}{v_a}\right)\right]. \quad (4)$$

Validation of Partitioned Wave Fields for a Finite Propagating Source

In this section, we demonstrate that upgoing and downgoing wave fields computed at a single depth can be used to predict the same rupture effect that is produced by a propagating rupture front along a vertical line source from one end to the other. In Figure 3, we show a set of theoretical

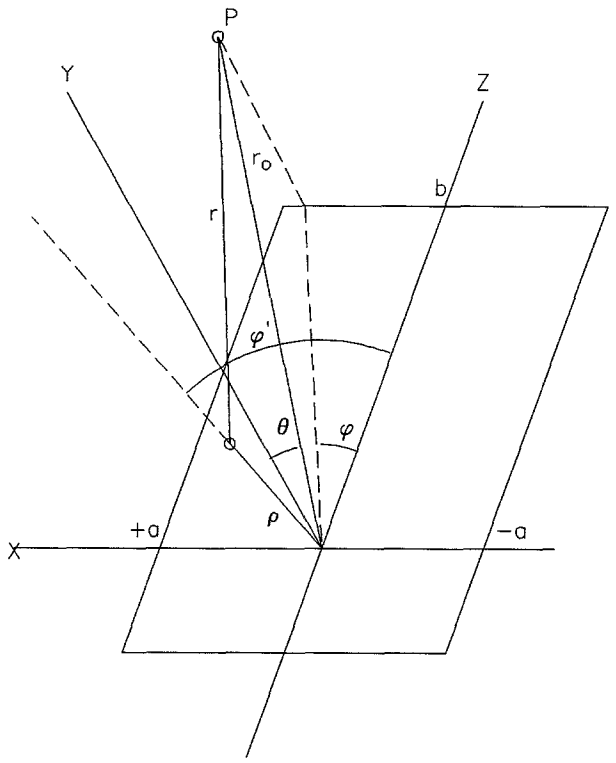

Figure 2. Coordinate geometry used to derive relations for a finite dislocation model (taken from Langston, 1978).

waveforms at a distance of 200 km from this line source. The upper trace is an equivalent point-source seismogram produced by averaging contributions from two point sources buried at depths of 9 and 10 km, with a time function shown to the right convolved in. The second trace includes rupture effects for the same size of event and is computed by including contributions from six point sources. The contributions are lagged in time based on a constant rupture velocity for the propagating rupture front that initiates at a depth of 12 km, continuing to a depth of 7 km. The third and fourth traces are generated, using the upgoing wave field for the third trace and the downgoing wave field for the fourth trace from a source buried at a depth of 10 km. Each wave field was convolved with a boxcar time function shown to the right. Note that the durations of the time functions are different for the two traces. Next, the third and fourth traces are summed to simulate the bottom seismogram. It is clear that the bottom seismogram has a better agreement with the second seismogram with rupture effect from six point sources than the top seismogram simulated using the point-source approximation.

The key to the success of producing the rupture effects by summing upgoing and downgoing wave fields lies precisely in how well the durations of the boxcar time functions are determined. To construct these time functions, a regional phase must be selected, which controls in shaping one of the principal features in the observed seismogram. For a simple

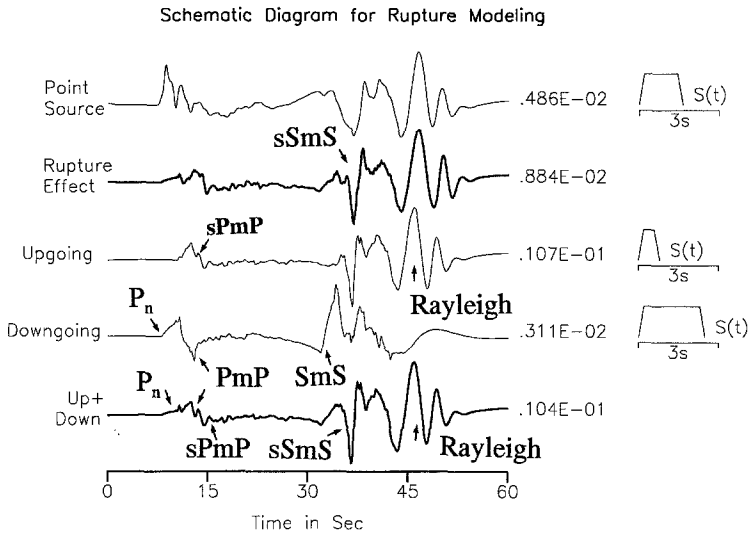

Figure 3. Schematic diagram showing seismograms produced by adding several point sources representing the rupture propagation along a fault 5 km long with a rupture velocity of 3.1 km/sec and by summing the upgoing and downgoing wave fields. The top seismogram represents a point-source seismogram synthesized by averaging contributions from sources at 9 and 10 km depths and convolving with the time function to its right. The second seismogram has rupture directivity from six point-source contributions. The third and fourth seismograms represent the upgoing and downgoing wave fields convolved with time functions analytically designed using rupture theory. The fifth seismogram is the sum of the third and fourth traces and has better agreement with the finite-source seismogram (second seismogram).

vertically propagating fault, the total duration of the time functions for the upgoing and downgoing wave fields should account for the time required by the rupture front to propagate along the fault as given by (4), the difference in the travel times needed by the regional phase to travel to a station from the two ends of the fault, and the duration of the slip function used for the point source in generating the rupture effect.

In Figure 4, the top seismogram generated using a smooth rupture propagation along a vertical line source is compared with the bottom six seismograms generated by summing upgoing and downgoing wave fields at six depths of 7, 8, 9, 10, 11, and 12 km. At each depth, the upgoing medium response was convolved with a time function whose duration is based on the *sPmP* wave, and the downgoing wave field was convolved with a time function whose duration is based on the *PmP* wave. It is important to note that the principal features of the long-period P_{nl} waves, the start of the *SmS* and the surface waves generated in the top seismograms, are well matched in the seismograms produced at each source depth by summing the partitioned wave fields. The *SmS* waveforms generated using the partitioned wave fields are also quite similar to those generated using the total rupture process. Similar agreement was also observed in the other fault types. Hence, the principal features, at least the shape, of some regional phases produced by the rupture propagation are insensitive to choice of depth at which the upgoing and downgoing wave fields are added, provided it lies within the fault surface.

A similar numerical experiment was performed using the time functions developed based on the travel times of the *sSmS* and *SmS* waves. We found that the differences in the waveforms generated using the *sSmS* and *SmS* waves to design the source time functions for the upgoing and downgoing wave fields, respectively, were quite subtle when compared with the waveforms presented in Figure 4. There was, however, an obvious difference in the peak amplitudes. For *sSmS* and *SmS* time functions, the peak amplitudes were large when the rupture propagated upward compared to the peak amplitudes simulated for the same rupture process using the *sPmP* and *PmP* waves. Exactly the opposite was observed when the rupture propagated downward and is consistent with the theoretical expectations.

Effects of Small Source Finiteness on High-Frequency Signals

The examples presented in the previous section are for large-sized earthquakes. Small earthquakes have smaller source dimensions and have larger corner frequencies. To investigate the source finiteness of small events, we simulated seismograms with a Nyquist frequency at 25 Hz assuming a rupture length of 1 km and allowed the fault to extend from 8 to 9 km. We simulated the rupture effect in the same way using six point sources with a separation of 0.2 km. In Figure 5, we demonstrate the applicability of the method at significantly high frequency. The time functions developed for the upgoing and downgoing wave fields using the *sPmP* and *PmP* waves, respectively, have smaller durations than those presented in Figure 3. The high-frequency *P* waves predicted by smooth rupture (second seismogram, shown by a dark line) is better simulated by the up + down wavefield (bottom seismogram) compared to the point-source simulation (top seismogram). Note how the various upgoing seismic phases, such as the *pPmP, sPmP, sSmS,* and Rayleigh waves in the upgoing wave field and the P_n, *PmP*, S_n, and *SmS* phases in the downgoing wave field, add as the two wave fields are combined to produce the up + down wavefield. The misfit in the *S* waves is produced due to the phase velocities of the *sPmP* and the *PmP* waves used to construct the durations of the source directivity functions. This misfit improves if *sSmS* and *SmS* phases are used to define the directivity functions. We generated a set of strike-slip seismograms, analogous to those shown in Figure 1.

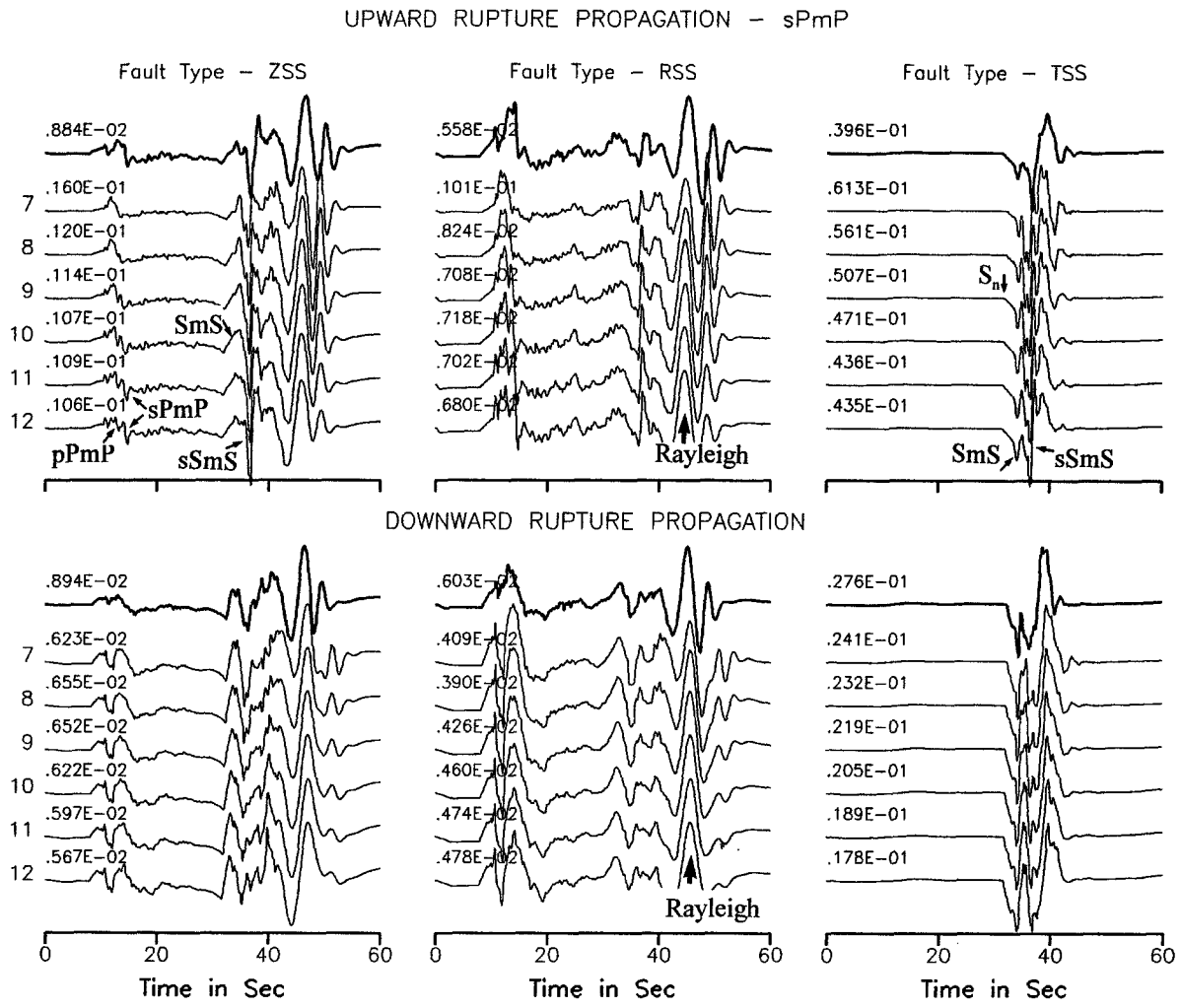

Figure 4. Upward and downward rupture simulated by summing the upgoing and the downgoing wave fields at various source depths, 7 through 12 km (southern California crustal model). The top seismograms have full representation of rupture directivity simulated by summing the contribution of six point sources. The next six seismograms are simulated by summing the upgoing and downgoing wave fields at each depth as discussed in Figure 3. Duration of the time function for the upgoing wave field is constrained by the travel times of *sPmP* waves and for the downgoing wave field by the travel times of *PmP* waves.

Unlike in Figure 1, both *PmP* and *sPmp* were strong pulses because the waves from individual sources add constructively with decreasing rupture dimension, thus increasing the relative strength of the high-frequency phases.

Application to Other Crustal Models

In this section, we summarize some additional results demonstrating that the proposed method is applicable to other crustal structures. We selected two models, one with increasing the thickness of the source layer by 5 km and the other with a low-velocity layer added to the top of the southern California model. The results for the model with increased layer thickness are shown in Figure 6. In this model, the durations for the time functions of different wave types remain the same as those used in the previous section, except for their absolute travel times. Their ray parameters change slightly due to changes in ray geometries, which results in changes in the reflection and transmission coefficients across the layer interfaces. This has an effect on the waveforms. For example, the *sPmP* phase for this modified model is stronger than the *sPmP* phase produced by the southern California model. In the next model, a 1-km-thick surface layer is introduced, having the *P*- and *S*-wave velocities of 1.8 and 0.9 km/sec, respectively, and a density of 2.6 gm/cm^3. The seismograms simulated using the responses from this model are shown in Figure 7. The acausal long-period noise is numerical and is due to the truncation of the low-frequency wavenumber imposed by the choice of wavenumber filter. As it can be seen in these waveforms, the model traps large

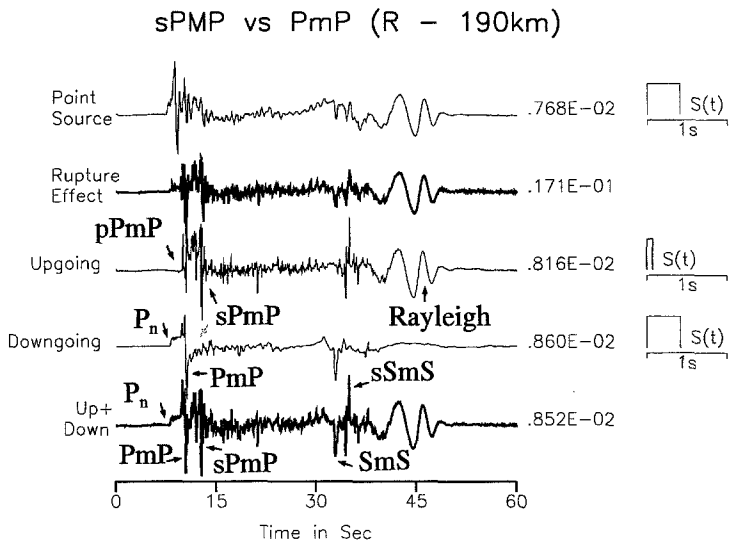

Figure 5. Schematic diagram to show the application of the method discussed in Figure 3 for high-frequency signals and for a small fault (has a dimension of 1 km). The seismograms are computed up to a Nyquist of 25 Hz. The point-source seismogram is simulated by using model responses computed at 8.4 and 8.6 km depth. The rupture effect is produced by using the same rupture velocity and the responses of six point sources at 8.0, 8.2, 8.4, 8.6, 8.8, and 9.0 km depth. Note the significant differences in the composition of *P*-wave signature as a function of fault size (Fig. 3 versus Fig. 5).

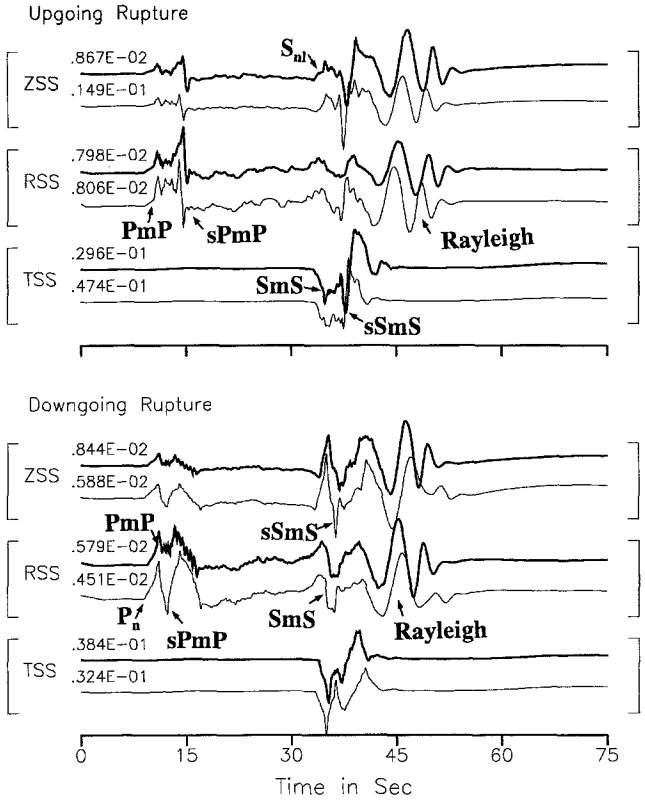

Figure 6. Sensitivity test of rupture directivity to the variation in the crustal structure model. Crustal thickness was increased by 5 km relative to the southern California model. The upper seismograms are simulated by summing point sources, and the bottom seismograms are simulated by summing the upgoing and downgoing wave fields.

surface waves, including well-dispersed P_{nl} waves that are also present on the point-source waveforms. We find the composition of both upgoing and downgoing P_{nl} waves complex. Individual wave groups are complex and have many high-frequency arrivals, and two groups interfere to produce longer-period wave train in the total field. This is consistent with our previous observation that introduction of low-velocity material near the surface causes perturbation in the free-surface and interface reflection and transmission coefficients resulting in a highly complex waveform (Saikia and Burdick, 1991). The model excited both Love and Rayleigh waves. The Rayleigh waves are complex for the model having low-velocity material near the surface, compared to the Rayleigh waves presented in the previous figures. The surface waves are long-period waves compared to the surface waves produced by the partitioned wave fields. This is expected because the rupture includes the surface waves from the shallower sources, i.e., the sources present at 7, 8, and 9 km, and those synthesized using the partitioned wave fields only consist of waves that are generated at 10 km. Also, the source time functions for the upgoing and the downgoing wave fields are based on the apparent velocities of the *sPmP* and *PmP* waves. The surface waves fit better when the rupture is downward because in this case, the duration of the time function for the upgoing wave field is longer, which effectively produces long-period surface waves.

However, the misfit in the long-period surface waves can be reduced by convolving the partitioned wave fields with the time functions developed for the *sSmS* and *smS* waves, as the time functions for the upward rupture of these

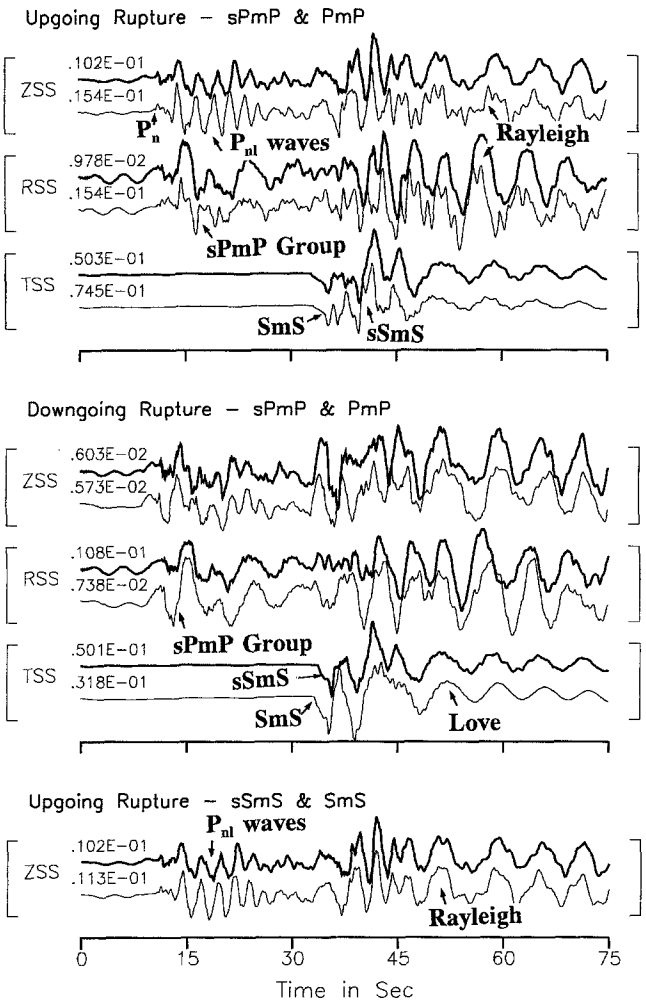

Figure 7. Sensitivity test of rupture directivity in presence of a low-velocity surface layer (thickness 1 km) in the crustal model. For each component, the upper seismogram has a full representation of rupture directivity, and the bottom seismogram is simulated by summing of upgoing and downgoing wave fields. Important to note is that there exists a mismatch in the long-period surface waves when the *sPmP* and *PmP* waves are used to constrain the durations of the time functions for the upgoing and downgoing wave field, respectively. The bottom two seismograms demonstrate the improvement in matching the long-period waves when time functions designed using *sSmS* and *SmS* waves are used.

waves have durations of 1.4 and 3.3 sec, respectively, longer than the durations of the corresponding *sPmP* and *PmP* waves, which are 0.8 and 2.5 sec, respectively. The bottom pair of seismograms are generated using *sSmS* and *smS* waves, and fit to the surface waves has improved significantly. Thus, unlike in the southern California model, the choice of regional phase may be crucial in simulating the rupture effects in presence of low-velocity material near the surface.

Summary of Numerical Procedure

In this section, we give a brief outline of how this method can be implemented in the routine source studies of broadband data. The following four steps will be the major tasks:

a. Generation of a crustal model capable of producing the dominant features generally observed on the recorded seismograms.
b. Construction of a library of upgoing and downgoing wave fields at various depths and distances.
c. Determination of the best-fitting point double-couple solution using long-period waves, see Saikia and Helmberger (1993), Dreger and Helmberger (1991), and Zhao and Helmberger (1993).
d. Simulation of the principal features in the broadband data, preferably in the high-frequency range, characterizing the rupture process on possible fault planes, iteratively searching for the best-fitting solution of the rupture velocity (v_r) and direction of rupture front propagation on the extended fault. A best-fitting solution will produce a minimum misfit between recorded data and seismograms simulated by adding the partitioned wave fields.

Conclusions

We have outlined an important application of separating wave fields into the upgoing and the downgoing components at source traveling to the regional distances and demonstrated that they can be used to investigate the source directivity manifested in the high-frequency data. The major contribution of this study is that a method is established that needs upgoing and downgoing partitioned wave fields at only one depth to simulate the principal features produced by rupture propagation on a fault. To compute the partitioned wave fields, we formulated a frequency-wavenumber algorithm capable of producing complete seismograms for the upgoing and downgoing wave fields using the Haskell (1964) formalism (Appendix A). The algorithm encompasses many numerical recipes that have proven quite effective. For example, it implements the normalization of the layer matrix elements including the compound matrices to avoid any need for specifying many thin layers to represent one large layer (Saikia, 1994; Herrmann and Wang, 1985; Wang and Herrmann, 1980; Herrmann 1979; Watson, 1970) and a larger wavenumber sampling interval using the Filon's quadrature to integrate the kernel at high frequency and at large distances (Saikia, 1994; Mallick and Frazer, 1988; Frazer, 1977). Presently, the method is demonstrated for the vertical line source, but the underlying concept can be extended to analyze rupture attributes on a large fault surface. The proposed approach is advantageous to other methods in which wave fields are computed at many points on the fault surface and is very well a major task, depending upon the frequency of interest and the epicentral distance.

To implement this method, it is imperative that regional phases that are recorded in the regional seismograms as the principal features are selected to construct the time functions, accounting the difference in travel times needed by the regional phase to travel to a station from the two ends of a fault and adding to the duration of the rupture front propagation. Generally, the *PmP, SmS, sPmP,* and *sSmS* waves are the primary candidates. These are reflected phases from the moho interface and contribute significantly compared to the direct waves for crustal earthquakes. At present, we have tested the implementation for the vertical line source and found that the upgoing and downgoing wave fields can be added at any depth, but they must lie within the fault dimensions.

We have verified the method using several flat-layered crustal structures. Path effects in a complex medium may complicate application of these results, especially when the fault dimensions are large and when the fault is buried within a highly irregular crustal structure. It is beyond the scope of this article to assess whether the summing of the upgoing and downgoing wave fields from one depth will be adequate for approximating the rupture effects for such large earthquakes. We can intuitively argue only for the small earthquakes as the fault dimensions are generally small. At least for such earthquakes, we can restrictively apply this approach to the initial high-frequency P waves even in the presence of irregular structure. Because the initial wave fields, produced by summing the individual point-source contributions that are influenced differently at different stations by the interaction with the complex irregular structure, are likely to have variations. However, wave fields from individual point sources will have similar interactions at a single site, producing similar looking wareforms. Thus, any upgoing and downgoing wave fields that include these complicated features of irregular structure will suffice for the method to perform.

Acknowledgments

We thank D. G. Harkrider of Seismological Laboratory, CIT, for his careful review of this manuscript, especially the mathematical formulation presented for the upgoing and downgoing waves. We also thank Chuck Ammons for his comments on this manuscript. Also, Robert B. Herrmann of Saint Louis University has helped to clarify many aspects of this wave-field partition formulation.

References

Bouchon, M. (1981). A simple method to calculate Green's functions for elastic layered media, *Bull. Seism. Soc. Am.* **71,** 959–971.

Dreger, D. S. (1994). Investigation of the rupture process of the 28 June 1992 Landers earthquake, utilizing TERRAscope, *Bull. Seism. Soc. Am.* **84,** 713–724.

Dreger, D. S. and D. V. Helmberger (1991). Complex faulting deduced from broadband modeling of the 28 February 1990 Upland earthquake (ML = 5.2), *Bull. Seism. Soc. Am.* **81,** 1129–1144.

Dunkin, J. W. (1965). Computation of modal solutions in layered, elastic media at high frequencies, *Bull. Seism. Soc. Am.* **55,** 335–358.

Frazer, L. N. (1977). Synthesis of shear-coupled PL, *Ph.D. Thesis,* Princeton University, Princeton, New Jersey.

Geller, R. J. (1976). Scaling relations for earthquake source parameters and magnitudes, *Bull. Seism. Soc. Am.* **66,** 1501–1523.

Gilbert, F. and G. Backus (1966). Propagator matrices in elastic wave and vibration problems, *Geophysics* **31,** 326–332.

Harkrider, D. G. (1980). Coupling near source phenomena into surface wave generation, in *Identification of Seismic Sources—Earthquake of Underground Explosion,* E. S. Husebye and S. Mykkeltveit (Editors), D. Reidael, Dordecht, 277–326.

Haskell, N. A. (1964). Radiation pattern of surface waves from point sources in a multilayered medium, *Bull. Seism. Soc. Am.* **54,** 377–393.

Hauksson, E., K. Hutton, H. Kanamori, L. Jones, and J. Mori (1994). The M_w 6.7 Northridge, California, Earthquake of January 17, 1994 and its aftershocks, *Seism. Res. Lett.* **65,** 241.

Helmberger, D. V. and D. H. Harkrider (1978). Modeling earthquakes with generalized ray theory, in *Modern Problems in Elastic Wave Propagation,* J. Miklowitz and J. Achenbach (Editors), Wiley, New York, 499–518.

Helmberger, D. V., R. Stead, P. Liu-Ho, and D. Dreger (1992). Broadband modeling of regional seismograms: Imperial Valley to Pasadena, *Geophys. J. Int.* **119,** 42–54.

Herrmann, R. B. (1979). S-wave generation by dislocation sources—A numerical study, *Bull. Seism. Soc. Am.* **69,** 1–16.

Herrmann, R. B. and C. Y. Wang (1985). A comparison of synthetic seismograms, *Bull. Seism. Soc. Am.* **75,** 41–56.

Kennett, B. L. N. (1983). *Seismic Wave Propagation in Stratified Media,* Cambridge Univ. Press, Cambridge, 342 pp.

Langston, C. A. (1978). The February 9, 1971 San Fernando earthquakes: a study of source finiteness in teleseismic body waves, *Bull. Seism. Soc. Am.* **68,** 1–29.

Mallick, S. and L. N. Frazer (1988). Rapid computation of multi-offset vertical seismic profile synthetic seismograms for layered media, *Geophysics* **53,** 479–491.

Saikia, C. K. (1994). Modified frequency-wavenumber algorithm for regional seismograms using Filon's quadrature—modeling of Lg waves in eastern North America, *Geophys. J. Int.* **118,** 142–158.

Saikia, C. K. and L. J. Burdick (1991). Fine structure of Pnl waves from explosions, *J. Geophys. Res.* **96,** no. B9, 14383–14401.

Saikia, C. K. and D. V. Helmberger (1993). Broadband modeling of regional seismograms in Asia and development of low-magnitude event discriminants, Scientific Final Report WCCP-R-93-04, Prepared for Phillip Laboratory, Kirtland Air Force Base, New Mexico, Contract Number F29601-91-C-DB01.

Saikia, C. K., B. B. Woods, L. Zhu, H. K. Thio, and D. V. Helmberger (1996). Path calibration, source estimation and regional discrimination for the Middle East: application to the Hindu-Kush Region, Scientific Report #1, PL-TR-96-2069, Phillips Laboratory, Hanscom Air Force Base, Massachusetts.

Savage, J. C. (1965). The effect of rupture velocity upon seismic first motions, *Bull. Seism. Soc. Am.* **55,** 263–275.

Savage, J. C. (1966). Radiation from realistic model of faulting, *Bull. Seism. Soc. Am.* **56,** 577–560.

Wang, C. Y. and R. B. Herrmann (1980). A numerical study of P, SV and SH wave generation in a plane layered medium, *Bull. Seism. Soc. Am.* **70,** 1015–1036.

Watson, T. H. (1970). A note on fast computation of Rayleigh wave dispersion in the multi-layered elastic half-space, *Bull. Seism. Soc. Am.* **60,** 161–166.

Zhao, L.-S. and D. V. Helmberger (1993). Source estimation from broadband regional seismograms, *Bull. Seism. Soc. Am.* **84,** 91–104.

Zhu, L. and D. V. Helmberger (1996). Advancement in source estimation techniques using broadband regional seismograms, *Bull. Seism. Soc. Am.* **86,** 1634–1641.

Appendix A

Partitioning of Wave Fields for a Point Source

To compute the upgoing and downgoing wave fields, we use the frequency-wavenumber integration scheme (Wang and Herrmann, 1980; Herrmann and Wang, 1985; Saikia, 1994) that follows from Haskell (1964) and construct time series by evaluating an integral of the type given by $\int_0^\infty F(k,\omega)J_n(kr)dk$, where ω is the angular frequency, k is the horizontal wavenumber, r is the epicentral distance, and J_n is the nth-order Bessel's function. The quantity $F(k,\omega)$ includes the vertical propagation of the frequency-wavenumber kernel that is evaluated using the propagator matrix technique (Gilbert and Backus, 1966), and the terms with Bessel's functions produce the horizontal wave propagation along the r direction. To separate upgoing and downgoing wave fields, we have to reconstruct $F(k,\omega)$. The kernel can be integrated either by using the criteria used by Bouchon (1981) or by using quadrature schemes like the Filon's quadrature to interpolate both $F(k, \beta)$ and $J_n(kr)$ (Frazer, 1977; Mallick and Frazer, 1988; Saikia, 1994).

Kennett (1983) presented a mathematical representation of two wave fields by partitioning the stress-displacement vectors immediately above and immediately below the source into their upgoing and downgoing wave parts using his inverse eigenvector matrix. The approach followed here is similar, but instead of the inverse matrix, the concept of the upgoing and the downgoing wave fields is applied to the frequency-wavenumber integration scheme using the source layer matrix $\mathbf{a}_m$, which implicitly has a form given by $\mathbf{a}_m = \mathbf{E}_m\mathbf{\Lambda}_m(\mathbf{z})\mathbf{E}_m^{-1}$ in terms of matrix propagator, $\mathbf{E}_m$ being a 4×4 matrix connecting the *P-SV* stress-displacement vector $\mathbf{B}_{m-1}$ to the potential constant vector $\mathbf{K}_m$ of the mth layer given by $\mathbf{B}_{m-1} = \mathbf{E}_m\mathbf{K}_m$. For *SH* waves, $\mathbf{E}_m$ is a 2×2 matrix. Matrix $\mathbf{\Lambda}_m(\mathbf{z})$ is composed of two matrices with elements consisting of exponential transfer operators for the propagating wave field within a layer (see below). Forms of both $\mathbf{E}_m$ and $\mathbf{E}_m^{-1}$ matrices are available in Haskell (1964). Such a decomposition of the propagator matrix aids in understanding individual upgoing and downgoing waves within a given layer and, in the limiting condition of layer thickness becoming zero, can be used to produce the upgoing and downgoing wave-field contributions.

The Haskell (1964) article introduced wave-field coefficients, $\mathbf{A}'$, $\mathbf{A}''$, $\mathbf{B}'$, $\mathbf{B}''$, $\mathbf{C}'$, and $\mathbf{C}''$, where **A**, **B**, and **C** coefficients are related to the propagating **P**, **SV**, and **SH** waves, respectively. The prime and double primes indicate association with downward and upward propagating waves, respectively. In an elastic medium [assuming a cylindrical coordinate system ($\mathbf{r}$, $\boldsymbol{\phi}$, $\mathbf{z}$) with the origin at the free surface and $\mathbf{z}$ pointing downward] consisting of $N - 1$ homogeneous and isotropic layers overlying a half-space (Nth layer) where each layer is characterized by the compressional (α) and shear wave (β) velocities, the density (ρ) and the thickness (d), Wang and Herrmann (1980) presented a compact form connecting the layer vector $\mathbf{K}_N$ of the Nth layer to the source potential discontinuities $\mathbf{K}_m^-$ and K_m^+ across the mth layer and the free-surface stress-displacement vector $\mathbf{B}_0$, which has a similar form as given below:

$$FK_N = X\Omega + RB_0, \tag{A1}$$

where

$$\begin{aligned} \Omega &= a_m(d_m = 0)\, E_m S, \\ X &= FE_N^{-1}a_{N-1}a_{N-2} \cdots\cdots a_{m+1}a_m(d_m), \\ R &= FE_N^{-1}a_{N-1}a_{N-2} \cdots\cdots a_1. \end{aligned} \tag{A2}$$

The layer matrix $\mathbf{a}_m(\mathbf{d}_m = 0)$ is essentially an identity matrix. The above expressions are in the exact form presented in Wang and Herrmann (1980) and Saikia (1994) and can be used to evaluate responses at receivers located at the free surface. The vector potential $\mathbf{K}_N$ is a 4×1 matrix given by $[\mathbf{A}' + \mathbf{A}'', \mathbf{A}' - \mathbf{A}'', \mathbf{B}' - \mathbf{B}'', \mathbf{B}' + \mathbf{B}'']^{\mathbf{T}}$ for the *P-SV* and is a 2×1 matrix given by $[\mathbf{C}' + \mathbf{C}'', \mathbf{C}' - \mathbf{C}'']^{\mathbf{T}}$ for the *SH* waves evaluated at the Nth layer. Matrix **F**, which is a 4×4 matrix for the *P-SV* system and a 2×2 matrix for the *SH* system, separates up- and downgoing wave potential coefficients in the **K** vector potential. Thus, $\mathbf{FK}_n$ is $[\mathbf{A}'', \mathbf{B}'', \mathbf{A}', \mathbf{B}']^{\mathbf{T}}$ for *P-SV* and $[\mathbf{C}'', \mathbf{C}']^{\mathbf{T}}$ for *SH* waves. The parameter d_m is the thickness of the layer immediately below the source. Thus, Ω is equivalently representative of the stress-displacement discontinuity at the source.

In Haskell's formulation, the layer matrix, $\mathbf{a}_m$ of the mth layer is defined as

$$a_m = D_m E_m^{-1}, \tag{A3}$$

which follows from the relations

$$B_m = D_m K_m \qquad B_{m-1} = E_m K_m. \tag{A4}$$

The first expression relates the stress-displacement vector $\mathbf{B}_m$ at the bottom of the layer m to the layer potential coefficient $\mathbf{K}_m$, and the second expression gives the stress-displacement vector $\mathbf{B}_{m-1}$ at the top of the same layer. The form of $\mathbf{D}_m$ matrix given in Haskell (1964) can be reformulated in terms of the $\mathbf{E}_m$ matrix as follows:

$$D_m = E_m(\Lambda_m^1 + \Lambda_m^2), \tag{A5}$$

where

$$\begin{aligned} \Lambda_m^1 &= \Lambda_m^{1^+} + \Lambda_m^{1^-}, \\ \Lambda_m^2 &= \Lambda_m^{2^+} + \Lambda_m^{2^-}. \end{aligned}$$

For the *P-SV* system,

$$\Lambda_m^{1\pm} = \frac{1}{2}\begin{vmatrix} e^{\pm \nu_\alpha d_m} & 0 & 0 & 0 \\ 0 & e^{\pm \nu_\alpha d_m} & 0 & 0 \\ 0 & 0 & e^{\pm \nu_\beta d_m} & 0 \\ 0 & 0 & 0 & e^{\pm \nu_\beta d_m} \end{vmatrix}, \tag{A6a}$$

$$\Lambda_m^{2\pm} = \frac{\pm 1}{2}\begin{vmatrix} 0 & -e^{\pm \nu_\alpha d_m} & 0 & 0 \\ -e^{\pm \nu_\alpha d_m} & 0 & 0 & 0 \\ 0 & 0 & 0 & -e^{\pm \nu_\beta d_m} \\ 0 & 0 & -e^{\pm \nu_\beta d_m} & 0 \end{vmatrix}, \tag{A6b}$$

and for *SH* system,

$$\Lambda_m^{1\pm} = \frac{1}{2}\begin{vmatrix} e^{\pm \nu_\beta d_m} & 0 \\ 0 & e^{\pm \nu_\beta d_m} \end{vmatrix}, \tag{A6c}$$

$$\Lambda_m^{2\pm} = \frac{\pm 1}{2}\begin{vmatrix} 0 & -e^{\pm \nu_\beta d_m} \\ -e^{\pm \nu_\beta d_m} & 0 \end{vmatrix}. \tag{A6d}$$

The matrix with the plus sign implies that the waves propagate upward, and that with the negative sign implies that the waves propagate downward. Thus, the layer matrix $\mathbf{a}_m$ can exactly be decomposed into layer matrices for the upgoing and downgoing waves. Hence, theory used in our algorithm is as follows:

$$\begin{aligned} \Omega &= a_m(d_m = 0)\, E_m S \\ &= E_m \Lambda_m(d_m = 0)\, E_m^{-1} E_m S \\ &= E_m[\Lambda_m^{\text{up}}(d_m = 0) + \Lambda_m^{\text{down}}(d_m = 0)]\, E_m^{-1} E_m S \\ &= [a_m^{\text{up}}(d_m = 0) + a_m^{\text{down}}\, d_m = 0)]\, E_m S = \Omega^{\text{up}} \\ &\qquad + \Omega^{\text{down}}. \end{aligned} \tag{A7}$$

To obtain these decomposed stress-displacement wave fields, Ω^{up} and Ω^{down}, using the elements of Haskell's layer matrix in which upward and downward propagations are introduced through $\exp[\pm \nu_{\alpha,\beta} d_m]$ terms, it is only necessary to evaluate the elements of the source layer matrix $a_m(d_m)$ in the limit when d_m tends to 0. This decomposition is an effective way to find coefficients needed to separate upgoing and downgoing components exactly from the stress-displacement wave-field discontinuity $E_m S$ at the source using the layer matrix itself. Following Harkrider (1980), a similar decomposition can be achieved in the source potential coefficients. Herrmann (personal comm., 1994) shows that the above decomposition is also equivalent to separating the source potential S into upgoing and downgoing source potentials as follows:

$$\begin{aligned} \Omega &= E_m S \\ &= E_m F^{-1}[FS] \\ &= E_m F^{-1}([F]^- S + [F]^+ S). \end{aligned} \tag{A8}$$

This formulation uses **F** matrix to achieve this separation. Both decomposition schemes have relative advantages in terms of computation and produce identical results.

Appendix B

Validation of Partitioned Wave Fields for a Point Source

One of the best demonstrations of the accuracy of our procedure is to simply add the upgoing wave field to the downgoing wave field and predict the point-source solution. This is shown in Figure B1 for the fundamental faults. The upper two panels show both upgoing and downgoing seismograms computed using the southern California crustal model, given in Table B1. The source is at a depth of 7 km. The distance of 200 km was chosen so that both the upgoing and the downgoing wave fields have similar amplitudes, making the contributions from both wave fields noticeable in the sum. At this distance, we expect the upgoing wave field to be composed primarily of strong high-frequency *pPmp* and *sSmS* waves and long-period surface waves. The *P-SV* interaction shows this to be the case for the upgoing wave field on the vertical and radial seismograms. The source is deep, which makes the tangential motions strong only at the high frequency. As expected, the downgoing wave fields are rich in high frequency and show complicated ray interactions within the *S*-wave packets. The *PmP* is strong on both strike-slip components. The lower two panels of Figure B2 show a direct comparison of the sum of the two wave fields (up + down) with the seismograms computed using the original frequency-wavenumber algorithm (Saikia, 1994) for the total field. The number to the right of each up + down seismogram gives the percentage of mismatch of the wave field produced by summing the upgoing and the downgoing wave fields with the total wave field, which is at most 0.5% (in fact, it is about 0.2% for the *P-SV* system). Since the upgoing and the downgoing wave fields are computed using a different numerical algorithm and the up + down result is the same as the total wave field, the algorithm used to partition the wave field into upgoing and downgoing components is validated.

We also compared the upgoing and downgoing wave fields computed by the above technique of wave-field partition with those computed using the generalized ray theory (Helmberger and Harkrider, 1978). Figure B2 shows the comparison of initial *P*-wave displacements computed using these two independent methods for both double-couple and isotropic sources buried at a depth of 10 km, and at a distance of 200 km for the *P-SV* waves. The calculation was done using a 40-km-thick layer over a half-space to keep ray tracking for the generalized ray seismograms simple and included only those generalized rays that significantly contribute to the total response. The *P*- and *S*-wave velocities within the layer are 6.2 and 3.5 km/sec and with a density of 2.7 gm/cm^3. The half-space parameters are 8.2 and 4.5 km/sec for *P* and *S* velocities and 3.4 gm/cm^3 for density. We computed generalized ray seismograms using only the far-field approximation for the upgoing and the downgoing wave fields separately and compared them with those computed

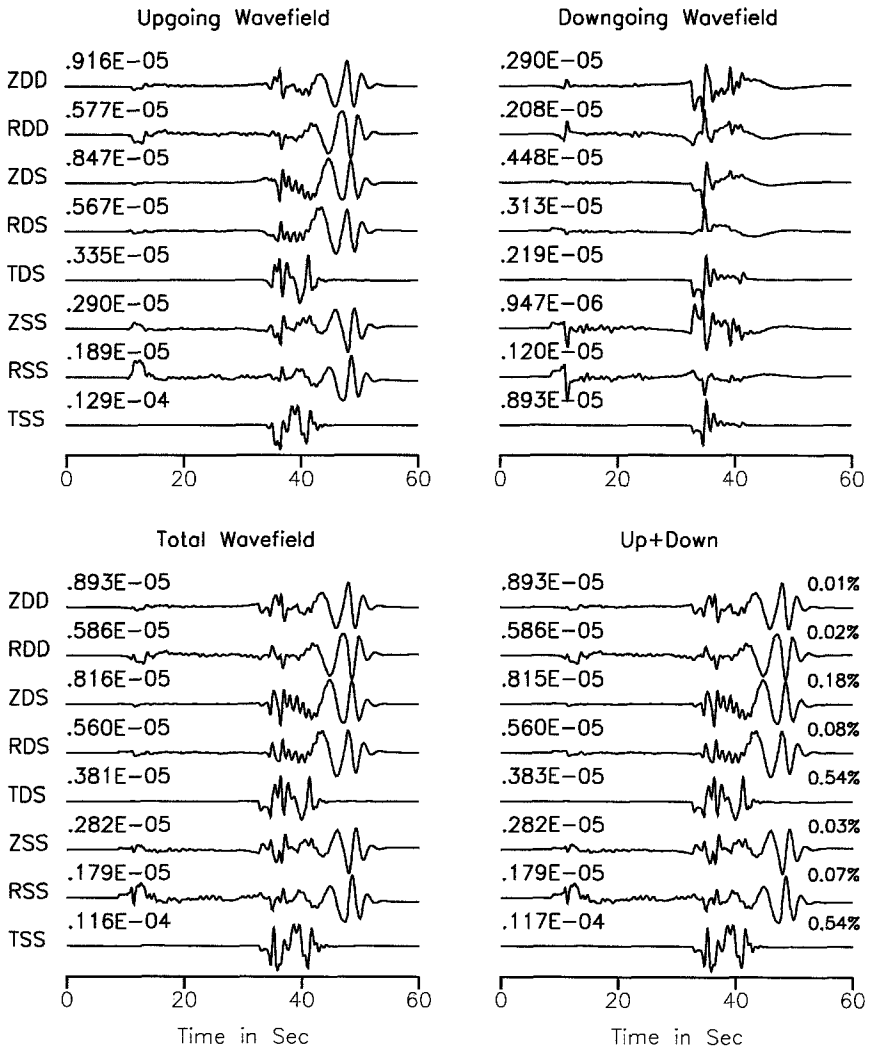

Figure B1. Separation of wave field into the upgoing and downgoing wave fields. The top panel shows the upgoing and the bottom panel shows the downgoing wave field. Source is 7 km depth and the southern California crustal model (Table B1) is used. The total wave field (bottom left panel) is computed by using Filon_AS (Saikia, 1994). The up + down wave field (bottom right panel) is produced by summing the up and down wave fields shown above. The number to the right of each up + down seismogram gives the percentage mismatch with the total wave field.

Table B1
Southern California Crustal Model Used in This Study

P Vel. (km/sec)	*S* Vel. (km/sec)	Density (gm/cm^3)	Thickness (km)
5.4	3.2	2.7	4.0
6.2	3.6	2.85	16.0
6.6	3.75	3.2	8.0
7.5	4.1	3.42	3.0
7.8	4.25	3.45	—

using the frequency-wavenumber algorithm for the partitioned wave fields. These upgoing and downgoing wave fields are shown in the first and second columns of seismograms. For each component, say *ZDD, RDD, ZDS, RDS, ZSS, RSS, ZEX,* and *REX* (where *Z* stands for the vertical component and *R* for the radial component, *DD* for the 45° dipping dip-slip fault observed at an azimuth of 45°, *SS* for the strike-slip fault and *DS* for the 90° dipping dip-slip fault, and *EX* for the explosion source), the generalized ray seis-

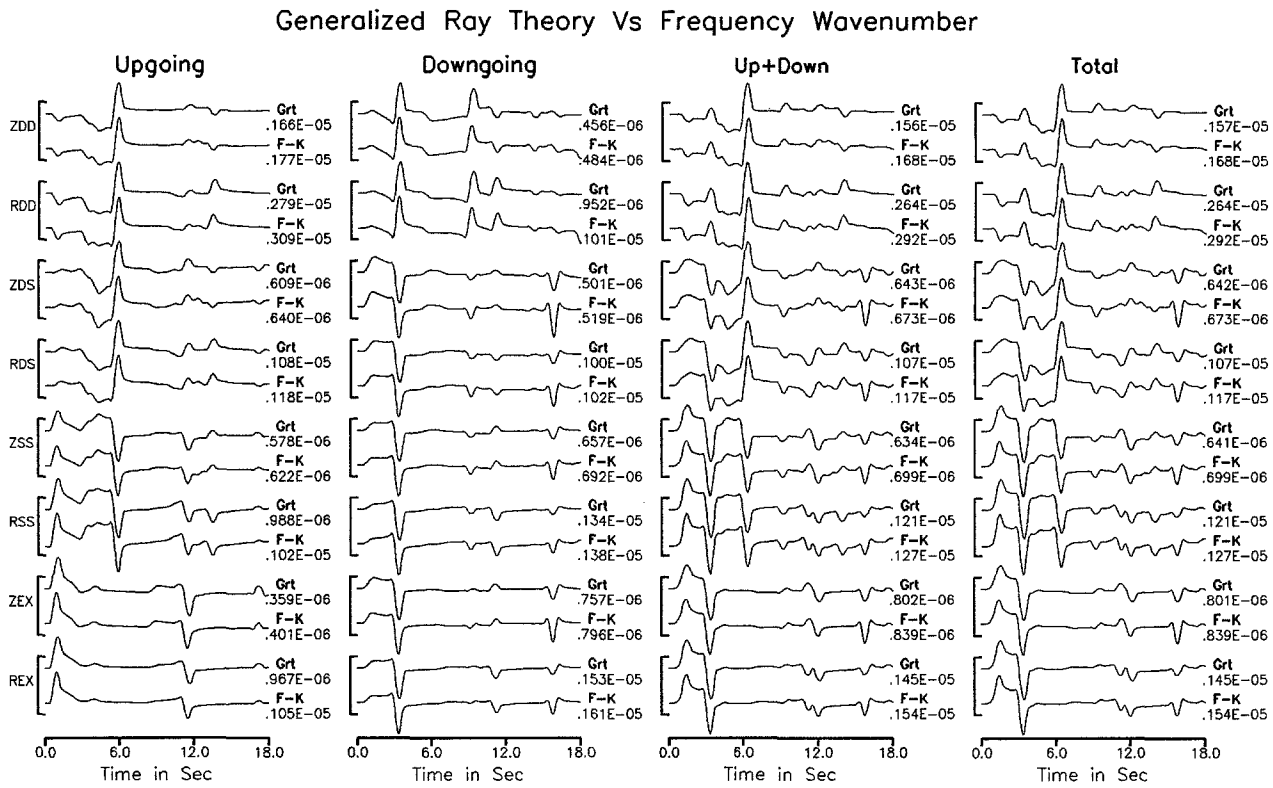

Figure B2. Comparison of generalized ray and frequency-wavenumber P_{nl} seismograms for the (a) upgoing, (b) downgoing, (c) up + down, and (d) total wave fields. The seismograms are synthesized using a layer-over-half-space model for a source depth of 10 km at a distance of 200 km. A limited number of rays are included in the generalized ray calculation. The total agreement between the seismograms shown in (c) and (d) both in amplitude and in waveshape validates the partitioned wave fields shown in (a) and (b).

mogram (Grt) is plotted above the frequency-wavenumber (*F-K*) seismogram. The peak amplitudes are also given. The small number immediately below the peak amplitude of *F-K* seismogram is the ratio of the peak amplitudes of the Grt to *F-K* seismograms, which ranges between 0.9 and 0.96. The seismograms in the Up + Down panel are synthesized by summing the upgoing and the downgoing wave fields of columns 1 and 2. The fourth column shows the total wave fields computed using all the rays together for the generalized ray seismograms and using the Filon_AS (Saikia, 1994) code for the *F-K* seismograms. The seismograms of the third column show an excellent match with the seismograms of the fourth column, both in amplitude and in wave shape. The agreement between the seismograms shown in columns 3 and 4 clearly validates the exactness of our method in partitioning the wave fields.

Woodward-Clyde Federal Services
566 El Dorado Street
Pasadena California, 91101, USA
(C.K.S.)

Seismological Laboratory
California Institute of Technology
Pasadena, California 91125, USA
(D.V.H.)

Manuscript received 14 March 1995.